

A Multi-Model Assessment of Evolving Forced Changes in Northern Hemisphere Modes of Atmospheric Circulation Variability and the Role of the Tropical Pacific

Nicola Maher, ^{1,2*}, Clara Deser³ and John P. O'Brien⁴

¹Research School of Earth Sciences, Australian National University, Canberra, ACT, Australia.

²ARC Centre of Excellence for Weather of the 21st Century, Australian National University, Canberra, ACT, Australia.

³Climate and Global Dynamics Laboratory, National Center for Atmospheric Research, Boulder, Colorado, USA.

⁴Heising-Simons Foundation, Los Altos, California, USA.

*Corresponding author(s). E-mail(s): nicola.maher@anu.edu.au;

Abstract

Understanding how modes of climate variability will change in a warming world is essential for improving regional climate projections. Using eight single model initial-condition large ensembles (SMILEs), we examine projected changes in the leading Northern Hemisphere modes of wintertime atmospheric circulation variability: the Pacific North American (PNA) pattern, the North Pacific Oscillation (NPO), the East Pacific Pattern (EPP), and the North Atlantic Oscillation (NAO), and their influence on precipitation. By applying a snapshot empirical orthogonal function (SEOF) analysis to the 500hPa geopotential height field in each SMILE, we are able to characterise how patterns, amplitudes, and impacts of each mode are projected to evolve over the next century. While most of the SMILEs generally capture the observed modes of variability, we find substantial disagreement in their projections of the NPO and NAO. The PNA response is more robust across models and is associated with a consistent intensification of the Aleutian low variability, which has implications for the volatility of future precipitation patterns over the United States. Both the PNA and NPO projections become more consistent between models when influences from the tropical Pacific are removed, highlighting that inter-model differences in projections of the

001
002
003
004
005
006
007
008
009
010
011
012
013
014
015
016
017
018
019
020
021
022
023
024
025
026
027
028
029
030
031
032
033
034
035
036
037
038
039
040
041
042
043
044
045
046

047 El Niño Southern Oscillation can confound projections of extra-tropical modes
048 of variability. In contrast, NAO projections remain model-dependent even when
049 tropical Pacific influences are removed. The EPP emerges as an increasingly
050 important mode for Californian precipitation in the future, with its influence
051 obscured by the tropical Pacific. Overall, our results demonstrate that there is
052 still much research to be done to better understand projected changes in modes
053 of climate variability and their impacts, given the large inter-model spread.

054 **Keywords:** ENSO, modes of variability, atmospheric circulation teleconnections, large
055 ensemble, snapshot EOF

056

057

058

059 1 Introduction

060

061 Understanding our climate requires information about both the mean state and the
062 variability around it. A key expression of such variability in the climate system is
063 through preferred patterns or "modes" that fluctuate between negative and positive
064 phases such as the North Atlantic Oscillation (NAO) and the El Niño Southern Oscil-
065 lation (ENSO). It is important not just to characterise these modes in present day
066 climate, but also their potential future changes. Previous research suggests that these
067 modes of variability are likely to undergo changes in their characteristics in response
068 to increasing greenhouse gas concentrations and global warming (e.g. [Branstator and
069 Selten, 2009](#); [Shepherd, 2014](#); [Deser et al, 2018](#)). Specifically, NAO variability is pro-
070 jected to strengthen under warming scenarios ([Visbeck et al, 2001](#); [Gillett et al, 2003](#);
071 [Deser et al, 2017](#); [Huang et al, 2018](#); [McKenna and Maycock, 2021](#)). This strengthen-
072 ing is expected to increase the frequency of extreme positive NAO winters and their
073 associated impacts in southern Europe ([McKenna and Maycock, 2021](#)). In contrast,
074 future changes in ENSO variability remain somewhat uncertain, although an increase
075 is suggested to be more likely than a decrease ([Maher et al, 2018](#); [Cai et al, 2021](#),
076 [2022](#); [Wengel et al, 2021](#); [Planton et al, 2024](#)). The spatial pattern of ENSO is also
077 expected to change under warming, although there is considerable uncertainty regard-
078 ing the nature of this change (e.g. [Maher et al, 2018, 2023](#)). Additionally, the Pacific
079 North American (PNA) pattern is projected to amplify ([Chen et al, 2018](#); [O'Brien and
080 Deser, 2023](#)) and shift its center-of-action northeastward ([Michel et al, 2020](#); [O'Brien
081 and Deser, 2023](#)). The linkage between the PNA and NAO may also strengthen in
082 the future by virtue of their mutual connection to ENSO ([O'Brien and Deser, 2023](#);
083 [Beverley et al, 2024](#)).

084 Teleconnections from modes of variability whereby a local perturbation results in
085 a remote response ([Wallace and Gutzler, 1981](#); [Barnston and Livezey, 1987](#); [Feldstein,
086 2000](#); [Feldstein and Franzke, 2017](#)), may also change in a warming climate. For exam-
087 ple, atmospheric teleconnections driven by ENSO may be modified in response to
088 changes in ENSO itself, and also to mean-state changes within the tropics and extrat-
089 ropics. For example, irrespective of changes in ENSO variance, precipitation variability
090 associated with ENSO in the tropical Pacific is expected to increase (e.g. [Power et al,
091 2013](#)) and shift eastward as the mean state warms (e.g. [Drouard and Cassou, 2019](#);
092

Zhou et al, 2014). In addition, mean-state changes in the position and strength of the midlatitude jet stream will alter ENSO-related teleconnections by modifying the sources and propagation characteristics of Rossby Waves. Indeed, ENSO teleconnections themselves are projected to change across approximately 50% of the globe, with most, but not all regions, experiencing an amplification of historical temperature and precipitation impacts (McGregor et al, 2022).

Understanding teleconnections and their projected changes, as well as what they mean for temperature and precipitation around the globe, is confounded by the lack of independence between different modes and their compounded impacts (e.g. O'Brien and Deser, 2023). For example, precipitation and temperature along the west coast of the United States are influenced by both the Pacific Decadal Oscillation (PDO) and ENSO (Maher et al, 2022), yet these modes are not independent of one another (Newman et al, 2016). Similarly, precipitation over Australia is affected by multiple modes of variability (Risbey et al, 2009), illustrating that understanding a single mode in isolation is not sufficient to fully explain local temperature and precipitation patterns. To further complicate matters, simply knowing the phase of each climate mode is often not enough to determine impacts. Indeed, modes of climate variability typically shift the likelihood of extreme events rather than serving as deterministic predictors (Maher et al, 2022). Despite these complexities, projecting changes in multiple modes of variability and their combined impacts remains essential for understanding the potential for extreme events and anticipating how local climate impacts are likely to evolve in the future.

To truly understand changes in variability and their time evolution in climate models, single model initial-condition large ensembles (SMILEs) are an invaluable tool (Deser et al, 2020; Kay et al, 2015; Maher et al, 2021a). These SMILEs are global coupled climate models, run with identical external forcing, identical model configuration, but different initial conditions for each ensemble member. The large number of ensemble members provides robust sampling of internal variability at any given time in each SMILE. As such these are ideal tools to investigate climate variability and its response to external forcing.

A novel method to quantify evolving characteristics of modes of variability is the Snapshot Empirical Orthogonal Function Analysis (or ensemble EOF; Haszpra et al, 2020; Herein et al, 2016; Maher et al, 2018; O'Brien and Deser, 2023). This method permits the use of EOF's to quantify modes of variability at any given interval in time, using samples from all members of a given SMILE. This approach thus enables the identification of how the amplitude and spatial characteristics of a mode may change in time due to external forcing. This method was applied assess forced changes in the leading patterns of wintertime atmospheric circulation variability over the Northern Hemisphere (NH) in the 40-member Community Earth System Model version 1 (CESM1) SMILE (O'Brien and Deser, 2023). They found that internal modes of circulation variability in the North Pacific and Atlantic amplify, expand their spatial footprint and produce enhanced precipitation impacts as greenhouse gas forcing increases. Notably, the third North Pacific EOF (the "East Pacific Pattern") demonstrated the largest forced changes in CESM1, which has important implications for the climate along the United States (US) west coast, and in particular, California.

139 These changes were driven by teleconnections from amplified ENSO activity in the far
140 eastern tropical Pacific and by intrinsic midlatitude atmospheric variability. Further-
141 more, the pattern of amplification of extratropical modes was found to resemble the
142 pattern of changes in the mean-state, highlighting the link between mean-state shifts
143 and variability.

144 One of the largest uncertainties in future projections of regional climate change
145 comes from model-to-model differences (Maher et al, 2021b), particularly for vari-
146 ability (van der Wiel and Bintanja, 2021; Lee et al, 2021). In this study we extend
147 the work of O'Brien and Deser (2023) to eight SMILEs from the new Multi-Model
148 Large Ensemble Archive v2 (Maher et al, 2025) to investigate structural uncertainty
149 in forced changes in leading modes of wintertime atmospheric circulation variability
150 over the NH and their precipitation impacts.

151

152 2 Methods

153

154 While a traditional Empirical Orthogonal Function (EOF) analysis computes modes
155 of variability across the time dimension of a single data set (observations or a single
156 realisation of a climate model or SMILE), the Snapshot EOF (SEOF) methodology
157 computes modes of variability across the ensemble dimension of a SMILE at each time
158 step independently (Haszpra et al, 2020; Herein et al, 2016; Maher et al, 2018; O'Brien
159 and Deser, 2023). Because each member of a given SMILE contains a unique sequence
160 of internal variability (once memory of the initial conditions has been lost), the phases
161 and amplitudes of a given mode are randomly distributed across the members, thereby
162 providing the SEOF analysis a wide sampling at any given instant in time. For exam-
163 ple, ENSO may be in a neutral, positive or negative phase, and may be strong or
164 weak, in different members of a SMILE at a given time. To isolate internal variability
165 in each member, the forced component is removed by subtracting the ensemble-mean
166 at each timestep. To compute SEOFs at each timestep of a given SMILE we apply
167 the following steps to the 500hPa geopotential height field in each member:

168

- 169 1. **Compute the December - February (DJF) seasonal mean for each year**
170 **of simulation.**
- 171 2. **Remove the ensemble mean** at each timestep to create anomalies (i.e.
172 departures from the forced response) due to internal variability.
- 173 3. **Apply a cosine latitude weighting** to account for variations in grid cell area
174 with latitude.
- 175 4. **Pool data from five consecutive DJF seasons** to increase sample size
176 (assuming stationarity over the 5-year window).
- 177 5. **Compute SEOFs** of the pooled data using the anomalies from all ensemble
178 members in a given SMILE.
- 179 6. **Assign the SEOF and its associated "Snapshot Principal Component"**
180 **(SPC) result** to the central year of each pooled window.
- 181 7. **Ensure consistent sign** of each SEOF mode across time using a pattern correla-
182 tion over the region of interest, correcting for potential ± 1 sign flips that can occur
183 in EOF analysis.

184

8. **Create global regression maps** by linearly regressing anomalies (departures from the ensemble mean) of the relevant climate variable at each timestep on the standardised SPCs.

This methodology replicates [O'Brien and Deser \(2023\)](#), with further details available in the original study. We apply this method to the eight SMILEs listed in Table 1 to investigate the following modes of variability:

North Pacific (20°–90°N, 110°–260°E):

- **Mode 1:** Pacific–North American pattern (PNA; [Barnston and Livezey, 1987](#))
- **Mode 2:** North Pacific Oscillation (NPO; [Linkin and Nigam, 2008](#))
- **Mode 3:** East Pacific Pattern (EPP; [Barnston and Livezey, 1987](#); [Yuan et al, 2015](#))

North Atlantic (20°–90°N, 80°W–10°E):

- **Mode 1:** North Atlantic Oscillation (NAO; [Hurrell et al, 2003](#))

We also compute the two leading SEOFs of tropical Pacific sea surface temperatures (35°S–35°N, 140°–295°E):

- **Mode 1:** First component of the El Niño Southern Oscillation (ENSO) ([Takahashi et al, 2011](#))
- **Mode 2:** Second component of ENSO ([Takahashi et al, 2011](#))

Table 1 SMILEs used in this study. Note that qualitatively similar results are found for ACCESS-ESM1.5 and CanESM5 in SSP585 as compared to the SSP370 results presented in this study (not shown)

Model	CMIP	Future Scenario	Members	time period	Reference
MPI-GE	5	RCP8.5	100	1850-2099	(Maher et al, 2019)
MIROC6	6	SSP585	50	1850-2100	(Tatebe et al, 2019)
IPSL-CM6A	6	SSP370	10	1850-2100	(Boucher et al, 2020)
GFDL-SPEAR-MED	6	SSP585	30	1921-2100	(Delworth et al, 2020)
CanESM5	6	SSP370	25	1850-2100	(Swart et al, 2019)
ACCESS-ESM1.5	6	SSP370	40	1850-2100	(Ziehn et al, 2020)
CESM1	5	RCP8.5	40	1920-2100	(Kay et al, 2015)
CESM2	6	SSP370	100	1850-2100	(Rodgers et al, 2021)

3 Results

3.1 A multi-model perspective on projected forced changes in circulation and precipitation variability

Building on the results of [O'Brien and Deser \(2023\)](#), we take a multi-model approach to investigate projected changes in circulation variability and their consequent impacts on precipitation. We first consider projected changes in circulation variability from

231 the early 20th century to the late 21st century across all 8 SMILEs before decom-
232 posing the changes into distinct modes and assessing model performance relative to
233 observations. Here, we define the early 20th century as the average of the SEOFs over
234 the period 1924-1934 and the late 21st century as the average of the SEOFs over the
235 period 2087-2097 (recall that the SEOFs are computed for each year separately using
236 pooled anomalies over a centred 5-year window). In the early 20th century all models
237 show hotspots of variability in the north Pacific and north Atlantic oceans that extend
238 onto the nearby land surface (Figure 1; first column). All models except MIROC6
239 project a robust strengthening of the Aleutian low variability with most models also
240 projecting a decrease in variability in the northern US and an increase in the south
241 (Figure 1; third column). These consistent signals across models appear in the multi-
242 ensemble mean (stippled regions in the bottom right panel of Figure 1). In contrast,
243 models show a lack of consistency in the Atlantic basin and European sector. Pro-
244 jected precipitation variability is largely consistent across models in both the Pacific
245 and Atlantic basins and over the entire North American Continent (Figure 2; agree-
246 ment shown in stippling) with an increase on both eastern and western US coastlines,
247 the North Pacific and mid latitude Atlantic, and generally all NH land masses. Con-
248 versely precipitation variance decreases in all models in both the subtropical Atlantic
249 and east Pacific. Changes in precipitation variability are due to the combination of the
250 changes in circulation variability and the mean effects of warming on the hydrological
251 cycle (e.g. enhanced water vapor content in regions of strengthened ascent in the extra-
252 tropics and deep tropics following the Clausius-Clapeyron relationship, and reduced
253 moisture in the subtropics due to enhanced subsidence). We suggest that the mean
254 effects of warming on precipitation variability dominate circulation-induced changes
255 in precipitation variability, given the more consistent stippling in Figure 2 compared
256 to Figure 1.

257

258 3.2 Modes of Circulation Variability: Model evaluation

259

260 Before examining future changes, we compare the simulated modes of Z500 variability
261 with observations to assess their realism. For this comparison we use a traditional EOF
262 approach (i.e. EOFs in time averaged across ensemble members) based on the period
263 1950-2015 so as to treat the SMILEs and observations in the same manner. However,
264 we note that the traditional and SEOF approaches yield very similar results for the
265 SMILEs (see Figure S2). All modes of variability are presented following the phase
266 conventions in O'Brien and Deser (2023). The spatial pattern of the leading EOF
267 in the North Pacific (PNA) and North Atlantic (NAO), obtained by regressing DJF
268 Z500 anomalies onto the correpronsing standardised PC timeseries, compares well with
269 observations in all eight SMILEs (Figure 3). The high pattern correlations (ranging
270 from 0.79-0.92 for the PNA and 0.85-0.94 for the NAO) between observations and each
271 SMILE attests to the realism of the simulated PNA and NAO structures. The second
272 mode in the North Pacific (NPO) is also well represented at the large scale, although
273 some discrepancies appear along the western US coastline. The pattern correlations
274 for the NPO are somewhat lower than those for the PNA and NAO (ranging from
275 0.7 to 0.84 across the SMILEs). Of the eight models, only MIROC6 captures both the
276 observed pattern and magnitude of the NPO, while ACCESS-ESM1.5 and CESM1 & 2

reproduce the correct pattern, but underestimate the magnitude. The third EOF in the North Pacific (EPP) is again captured at the large scale, but model results differ from each other and from observations, with models generally displaying a westward shift in the pattern relative to the observed one (pattern correlations range from 0.02-0.71).

While the large-scale patterns are generally well captured for all North Pacific and North Atlantic modes considered, it is important to recognise that observations represent just one realisation of the climate system (Maher et al, 2025). Therefore, to make a fair comparison with the SMILEs, we must assess whether any individual ensemble member resembles observations rather than considering just the mean across members. This comparison is shown in the Taylor diagrams in Figure 4. For the PNA, NPO and NAO, all models have ensemble members that match observations well across all metrics (correlation coefficient, standard deviation, and RMSD) highlighting that all models well-represent these modes of variability. Specifically, for both the PNA and NPO, CESM2, MPI-GE, ACCESS-ESM1.5, CESM1, and GFDL-SPEAR have members close to the observations (correlation coefficients greater than 0.9, similar standard deviations to observations and RMSD below 5). For the NAO, all models have ensemble members that are close to observations, except for CanESM5 in which all members have RMSD larger than 7.5, too high standard deviations, and correlations lower than 0.95, while all other models have members higher than 0.95. For the EPP, there is a wide range of correlation values across the members of each SMILE (ranging from negative to positive), suggesting that this mode is less well-constrained (i.e. we may need a longer record to sufficiently capture this mode in observations). Even so, all models have members relatively close to observations (similar standard deviations, correlation coefficients around 0.9, and RMSD less than 5) except CESM1 and ACCESS-ESM1.5. We note that observations are just one realisation and as such if some members have low correlations with observations it does not mean they do not well represent observations. If other members of a SMILE show high correlations, then this model can be considered to have a realistic representation of the mode in question, subject to uncertainties due to limited sampling.

Overall for all models considered, while biases exist, nearly all models have ensemble members that compare well with observations, and no single model clearly outperforms or underperforms compared to the others. Therefore, we include all eight SMILEs in our subsequent analysis to capture a robust range of future projections and identify areas of model agreement.

3.3 Modes of Circulation Variability: Projected changes

To understand what drives the projected changes in circulation and precipitation variability shown in Figures 1 and 2, we apply the SEOF method to identify dominant modes of NH Z500 variability and investigate their projected changes (Figure 5). For each mode, the positive phase in the early period (1924-1934) is shown as contours, and the difference between the positive phase in the late period (2087-2097) and positive phase in the early period is shown as color shading. For example, for SEOF1, dashed contours and blue shading over the North Pacific region indicate that the positive phase of the PNA during the early period (characterised by a deeper-than-normal Aleutian Low) is projected to intensify (become even deeper), and vice versa

323 for the negative phase. The main center of action of the PNA is projected to intensify
324 in all models except CESM2 and MIROC6, although the amplitude of the projected
325 amplification varies considerably across models (smallest for ACCESS and largest for
326 IPSL-CM6A). Remote linkages over the North Atlantic and European sector are highly
327 model dependent. To summarize the robustness of the projected changes across the 8
328 SMILEs, we compute a signal-to-noise ratio (S/N) defined as the multi-model mean
329 change divided by the standard deviation across models. A S/N value exceeding 1
330 highlights regions where there is high inter-model agreement on the projected change
331 relative to the spread across models. For the PNA the S/N exceeds 1 over the northern
332 portion of the North Pacific and exceeds 2 over the Gulf of Mexico and Florida. We
333 note that the MEM and S/N are qualitatively similar when MIROC6 and CESM2
334 are removed (not shown), highlighting that it is not just these outliers that drive the
335 model differences. Large inter-model differences are found in the Atlantic, where the
336 projected influence of the PNA is inconsistent.

337 The NPO, shows substantial model disagreement in its projected circulation
338 impacts over the Pacific and the continental US. For example there is a strong intensi-
339 fication of its influence over Alaska in CanESM5 and MPI-GE, but a small weakening
340 in MIROC6 and CESM1. Some models (e.g. CESM2, CESM1, GFDL-SPEAR and
341 MIROC6) show an intensification of the circulation over the south-eastern US related
342 to the NPO while the other models show a weakening (e.g. MPI-GE and CanESM5).
343 The influence of the NPO on the Atlantic, however, appears relatively consistent with
344 a strengthening influence in the mid-latitudes and a weakening in both the tropics and
345 high-latitudes further demonstrated by the S/N exceeding 1 in this region. This mode
346 also has increasing links to the tropics again demonstrated by the S/N larger than 1.

347 For the EPP there is some agreement among models, particularly over the west
348 coast of the US associated with a projected eastward shift of the pattern, highlighted
349 by the zonal dipole of high S/N between the Pacific and western US. Finally, the
350 NAO exhibits high inter-model variability in its projected changes, especially over the
351 Atlantic, as indicated by a low S/N in this region. Specifically, CanESM5 and IPSL-
352 CM6A show similarities in the change with a strong weakening of the NAO circulation
353 (red region highlighting a decrease due to the sign of the historical circulation), how-
354 ever the other models show weaker and inconsistent changes in sign across the region.
355 This is likely the cause of the model differences found in Figure 1 in the Atlantic.
356 Interestingly, projected changes in NAO variability are consistently linked to a pro-
357 jected intensification of Aleutian Low variability associated with the PNA and to the
358 enhanced variability in the tropics, with S/N values exceeding one in these areas. This
359 highlights the bi-directional link between the Atlantic and Pacific as shown by the
360 influence of the changes in the North Pacific EOFs on the Atlantic and visa versa,
361 which are different in strength in each model.

362 Changes in atmospheric circulation variability lead to corresponding shifts in local
363 precipitation variability. To explore these impacts, we regress precipitation onto the
364 Z500 SPCs and plot the change in the regressed precipitation field in the late compared
365 to early period (Figure 6). The projected intensification and eastward-shift of the
366 Aleutian Low center-of-action of the PNA pattern leads to enhanced precipitation
367 variability over the eastern North Pacific and along the west coast of the US and
368

diminished precipitation variability over the central North Pacific in most models. This signal is notably absent in MIROC6, where the Aleutian Low variability does not increase. The magnitude of the projected precipitation variability increase has high S/N showing the MEM change is larger than the model differences. The Pacific sector of the Arctic is another region of high S/N (values greater than 2), indicative of a robust reduction in precipitation variability associated with the PNA in the future. In line with the lack of model agreement in the projected behaviour of the NPO over the eastern North Pacific and North America, NPO-related precipitation changes in these regions also vary substantially between models, reflected in low S/N. However, the consistent NPO projections over the far western Pacific centered near Japan and over the North Atlantic produce robust (S/N greater than 1) signals in precipitation variability along the Kuroshio Extension and in a meridional dipole pattern over the North Atlantic. The high degree of model consistency in projected EPP variability is evident in the associated precipitation impacts, with most models projecting a banded structure of increased precipitation variability along the US West Coast, extending southwestward to Hawaii, decreased precipitation variability from British Columbia to the central north Pacific, and enhanced variability in the far northwestern Pacific. These changes likely stem from shifts in the jet stream position, supported by the shift in precipitation across the Pacific seen in both individual models and the MEM. We note that the details of the location of this change are shifted somewhat in each model, resulting in the S/N being lower than expected in this region. While there is a lack of model consensus on the projected changes in NAO-related precipitation variability over the central and northern North Atlantic, consistent with the Z500 field itself, the southwestern North Atlantic and the Pacific near Hawaii are regions of strongly robust (S/N greater than 2) changes.

One of the advantages of the SEOF method is that projected changes in the characteristics of internal variability can be evaluated continuously through time. In Figure 7 (left and right columns), we present the total and explained variance of each Z500 mode as a function of time from the beginning of each simulation until the end of the century. In the North Pacific, total Z500 variance increases continuously in all models except ACCESS-ESM1-5 and MIROC6, where it initially increases but subsequently declines (red curves Figure 7, left column). The proportion of variance explained by each of the three North Pacific Z500 modes remains relatively stable over time, although the PNA shows an increase in most models (excluding ACCESS, IPSL-CM6A and MIROC6 where it stays relatively stable). In contrast, the NAO exhibits less agreement across models, with some showing increasing total variance (CESM1 with a 15% increase, MIROC6 with 10%), others a decreasing (CESM2 with a 10% decrease, ACCESS with 15%, CanESM5 with 20%), and some showing little change (GFDL-SPEAR, IPSL-CM6A and MPI-GE). Despite these differences, the percentage of the variance explained by the NAO remains fairly stable across all models over time.

3.4 Role of the Tropical Pacific

Models show substantial differences in their projections of ENSO (Maher et al, 2023), which could contribute to the differences in their future circulation changes, as ENSO teleconnections can project onto the NH modes of variability (O'Brien and Deser,

415 2023). These model differences in ENSO projections are highlighted in Supplementary
416 Figure S9 (left hand side). In particular, the different models show contrasts in sign
417 in their projected surface temperature changes in the tropical Pacific as well as low
418 signal to noise in the region. We note that the precipitation related changes to these
419 modes in the tropical Pacific are much more consistent (Supplementary Figure S9;
420 right hand side), as noted in previous work (Power et al, 2013). The total variance
421 (Figure 7) of tropical Pacific SST EOFs broadly agrees with (Maher et al, 2023)
422 who found that most models exhibit a time-dependent increase in tropical Pacific
423 SST variability. While most models show a projected increase in tropical Pacific SST
424 variability, notable exceptions include MPI-GE, which shows no change, and CESM2
425 and GFDL-SPEAR, which increase and then decrease, with CESM2 returning to its
426 1850 amplitude by the end of the century from a high in the 2020s. Interestingly,
427 several models show a plateau in variance at the end of the record, suggesting a
428 possible future decline if simulations were extended. The variance explained by each
429 EOF tends to follow the trajectory of total variance.

430 To investigate how changes in the tropical Pacific modes impact the extratropical
431 Z500 modes, we linearly regress the Z500 anomalies over the NH onto the two leading
432 standardised SPCs of tropical Pacific SSTs at each timestep. and then remove this
433 contribution from the Z500 field following O'Brien and Deser (2023). We then recom-
434 pute the Z500 SEOFs using this residual field from which the tropical Pacific influence
435 has been removed. We find that for all models, the total variance of the "tropical
436 Pacific removed" Z500 anomalies over the North Pacific is substantially reduced com-
437 pared to the full Z500 anomalies, while the percent variance explained by each SEOF
438 mode remains similar (Figure 7, dashed curves in the left column). In the Atlantic, the
439 total variance during the historical portion of the simulations decreases only slightly
440 without the influence of the tropical Pacific, while the future variance is significantly
441 reduced (in all models except IPSL-CM6A and MIROC6), suggesting that the tropical
442 Pacific's influence on the Atlantic intensifies in future projections across all models.
443 Similar to the Pacific modes, the percent variance explained by the NAO is relatively
444 insensitive to the removal of tropical Pacific influence in all models (Figure 7, right
445 column).

446 Figure 8 shows the spatial patterns of Z500 and precipitation regressed onto the two
447 leading standardized SPCs of tropical Pacific SSTs (TPac) in the early period (con-
448 tours) and their future change (late minus early periods; shading) in each SMILE and
449 the MEM. While the early period Z500 teleconnection associated with TPac SEOF1 is
450 robust across models and resembles the PNA pattern, the projected change in the tele-
451 connection shows substantial model disagreement in both pattern and sign (Figure 8,
452 left column). Notably, CESM2, GFDL-SPEAR and MIROC6 show a future weakening
453 of the teleconnection variability (denoted by positive Z500 variability values; red shad-
454 ing) over the central North Pacific while CanESM5, IPSL-CM6A and MPI-GE show
455 the opposite behaviour. This does not appear to be linked to the change in variance in
456 the TPac (Figure 7). Model differences in the sign of the future changes in Z500 vari-
457 ability are also found over the North Atlantic. As highlighted in the S/N maps, model
458 differences in future Z500 variability changes associated with TPac SEOF1 are largest
459 over the western and central North Pacific (low S/N) and smallest in the eastern North
460

Pacific, southeastern US and across the Atlantic along around 30N and approximately 461
60N (high S/N). Corresponding differences are found in the precipitation responses 462
(Figure 8; third column), which show large model differences in the same regions as 463
the model differences in circulation. In contrast, TPac SST SEOF2 shows more con- 464
sistent behaviour in projected changes in its Z500 teleconnections across models with 465
enhanced Z500 variability in the Aleutian Low region (Figure 8; second column) with 466
high S/N. This in turn corresponds to increased precipitation variability along the 467
southwestern US coast (Figure 8; far right column), which also has a high S/N ratio. 468

Given the lack of independence between tropical Pacific SST SEOFs and NH Z500 469
SEOFs, and the large model differences in tropical Pacific projections outlined above, 470
we test whether these tropical differences drive the spread in projections of leading 471
modes of Z500 variability over the NH. To do so, we compare the projected changes in 472
the SEOFs based on the full Z500 field with those obtained from the residual Z500 field 473
after removing the influence of the tropical Pacific SST SEOFs via linear regression. 474
Results from the individual SMILEs are shown in Figures S10 & S11. Here we focus 475
on the MEM results (Figure 9). The projected amplification of the MEM PNA is 476
considerably reduced when the influence of the tropical Pacific is removed (Figure 9, 477
upper two panels in the left column). The multi-ensemble standard deviation (ME- 478
STD), which reveals where models differ most in their projections also decreases when 479
the tropical Pacific is removed, not only over the North Pacific and North America, 480
but also over the North Atlantic (Figure 9, middle two panels in left column). Given 481
that both the signal and noise reduce for the PNA, the S/N over the North Pacific is 482
largely unchanged; however, the S/N increases across the eastern US, tropical North 483
Atlantic and northern Europe due mainly to a reduction in the noise rather than an 484
augmentation of the signal (Figure 9, lower two panels in the left column). We find 485
a similar story for the PNA driven precipitation (Figure 10), although in this case 486
the S/N increases over the North Pacific and western Arctic and decreases over the 487
western US when the tropical Pacific influence is removed. 488

For the NPO, removing the influence of the tropical Pacific decreases the S/N 489
in the Atlantic region and throughout the tropical belt due to a stronger reduction in the 490
MEM signal compared to the ME-STD noise (Figure 9, second column). While the 491
NPO driven precipitation also shows a decrease in the S/N over the Atlantic sector 492
when the tropical Pacific influence is removed, due to a larger decrease in the signal 493
than the noise, there are also slight increases in S/N over the Gulf of Alaska and the 494
eastern US seaboard (Figure 10, second column). 495

For the EPP, removing the tropical Pacific influence reduces the S/N over western 496
North America as a result of the larger increase in noise than signal, while it increases 497
the S/N over the eastern US and tropical North Atlantic as a result of reduced noise 498
and larger signal, for both circulation and precipitation (Figure 9 & 10, third column). 499

For the NAO, removing the tropical Pacific influence slightly augments the S/N 500
in the circulation centres-of-action over the western North Atlantic and European 501
continent due mainly to the enhanced signal, while it greatly reduces the S/N over 502
the North Pacific and the tropical belt due to the decreased signal (Figure 9, far 503
right column). Analogous results are found for NAO-related precipitation, although 504

505
506

507 the increase in S/N over the Atlantic/European sector is not as apparent (Figure 10,
508 far right column).

509 We summarize the magnitude of the future change in each Z500 SEOF mode, with
510 and without the influence of the Tropical Pacific, based on the MEM (Figure 11). The
511 magnitude of future change is quantified by computing the spatial root mean square
512 (RMS) of the future change in Z500 regressions (shaded fields in the upper two rows
513 of Figure 9 for the MEM) over the domain used to define the SEOF (North Pacific
514 or North Atlantic). For the MEM PNA the magnitude of the circulation variability
515 is projected to increase, with approximately half of the increase due to the influence
516 of the tropical Pacific. In contrast, the MEM NAO is projected to weaken, and the
517 tropical Pacific influence approximately doubles the amplitude of the weakening. The
518 projected increase in the magnitude of the MEM NPO, although smaller than that of
519 the PNA, is more than doubled when the influence of the tropical Pacific is removed.
520 Finally, while the EPP RMS is projected to decrease this is found to be entirely due to
521 the tropical Pacific with no changes remaining after it's removal. Thus, future changes
522 in tropical Pacific SST variability exert a large influence on future changes in the
523 amplitude of the MEM Z500 SEOF modes, augmenting the PNA, offsetting the NPO
524 and NAO, and dominating the EPP.

525

526 **3.5 Impacts on Californian and South-Eastern US** 527 **precipitation variability** 528

529 We additionally consider the impacts of each Z500 mode of variability on Califor-
530 nian precipitation variability to assess whether the projected changes in precipitation
531 variability are consistent across models. We find a projected increase in Californian
532 precipitation variability associated with the PNA and NAO (Figure 12; left), about
533 two-thirds which is directly attributable to changes in tropical Pacific SST variability
534 for both modes. In contrast, projected changes in the NPO exert only a minor influ-
535 ence on Californian precipitation variability, regardless of whether the tropical Pacific
536 influence is removed or not. Projections of precipitation variability driven by the EPP
537 are as large as those due to the PNA when the influence of the tropical Pacific is
538 included. When the confounding influence of this region is removed, an even larger
539 increase in Californian precipitation variability emerges due to the EPP alone. This
540 suggests that the projected increases in Californian precipitation variability attributed
541 to the PNA and NAO are in fact driven in large part by non-independent changes
542 in tropical Pacific SST variability whose associated Z500 teleconnections project onto
543 these modes. Conversely, the tropical Pacific masks approximately one-third of the
544 signal from the EPP, highlighting that the EPP itself is projected to drive increased
545 volatility of Californian precipitation variability in the future. We also consider the
546 south-east US (Figure 12; right) which shows contrasting results to Californian pre-
547 cipitation variability. An increase in precipitation variability in this region due to the
548 PNA, EPP and NAO and a decrease due to the NPO are all found to be related to
549 tropical Pacific changes. When the tropical Pacific is removed, the PNA and NAO
550 changes switch to a decrease of the same magnitude, the NPO change results in an
551 increase of two-thirds the magnitude of it's original decrease, and the EPP influence
552

is reduced to one-third of its original magnitude. These results highlight the key role of the tropical Pacific in masking the influence of the other modes in this region.

4 Discussion

While our results show that the SMILEs considered in this study generally perform well in simulating the leading modes of wintertime circulation variability in the NH during the period 1950-2015, we find that this alone is not sufficient to ensure consistent projections of these modes and their associated impacts over the 21st Century. Where model disagreement is evident (in particular in the NPO and NAO), it reflects our ongoing inability to fully understand and simulate the processes that will change under warming. This highlights the continued need for a diversity of climate models to adequately capture the range of possible futures, especially in areas where our understanding is currently limited. Longer observational records will help improve model evaluation and allow for better quantification of internal variability and updated evaluation methods (Suarez-Gutierrez et al, 2021; Simpson et al, 2025), while higher-resolution simulations may better capture key processes (Wengel et al, 2021; Chang et al, 2026). However, our understanding remains incomplete regarding the precise sources of model differences. In this paper, we identify the large differences in the projected changes in SST variability in the tropical Pacific (e.g. ENSO) as a key driver of model differences in projected changes in Z500 variability over the NH, but also show that they are not the only source of discrepancy.

The SEOF approach applied to SMILEs provides a direct and concise way to assess forced changes in modes of circulation variability as highlighted by O'Brien and Deser (2023). While informative O'Brien and Deser (2023) was limited to one particular SMILE (CESM1), leaving open the possibility that different SMILEs might behave differently. We address this gap in our study and also evaluate model realism in simulating modes of variability over the historical record using the traditional time-EOF approach. Similar to previous studies (Michel et al, 2020; Chen et al, 2018; O'Brien and Deser, 2023), we find a projected future strengthening and north-easterly shift of the variability of the Aleutian low associated with the PNA pattern in all models except MIROC6 (see Figure 5), highlighting a broad consistency across models. When the influence of the tropical Pacific is removed, the spread in projections decreases, indicating that some of the inter-model differences, particularly in the Aleutian low region, are driven by inconsistencies in how the tropical Pacific is changing. Notably, the increasing influence of the PNA on Californian precipitation variability is found to be driven in large part by the tropical Pacific in the MEM (Figure 12). When isolated, the intrinsic atmospheric PNA changes themselves have limited impact on Californian precipitation, reinforcing the importance of accounting for interactions between modes of variability in future projections to truly understand what drives what.

Our results showing model disagreement in the projections of the NPO are consistent with previous work using CMIP5 models, further highlighting persistent uncertainty in this mode (e.g. Chen et al, 2018, 2021). Removing the influence of

599 the tropical Pacific leads to greater consistency in both circulation and precipita-
600 tion projections across models, particularly over the western US coastline, Alaska,
601 and the continental US. However, even with the tropical Pacific influence removed,
602 notable model differences remain. This suggests that uncertainties in the NPO’s future
603 behaviour stem from factors beyond tropical Pacific variability and that further work
604 is needed to better understand the processes driving the NPO and how they may
605 change under warming.

606 Similar to the findings of [O’Brien and Deser \(2023\)](#), we diagnose an important role
607 for the EPP in influencing precipitation along the western US coastline. Markedly, this
608 mode drives precipitation variability changes that are not solely driven by the tropical
609 Pacific. In particular, for the EPP, we find a consistent increase in its influence on
610 Californian precipitation in the future across all models, a response that is clouded by
611 the tropical Pacific influence. This result, again in line with [O’Brien and Deser \(2023\)](#),
612 points to a growing importance of the EPP for US regional hydroclimate under future
613 climate change.

614 The NAO also exhibits substantial discrepancies in future projections across mod-
615 els, consistent with previous work (e.g. [Smith et al, 2025](#)). These discrepancies cannot
616 be attributed to tropical Pacific influences, indicating that the differences arise from
617 the NAO projections themselves. All models suggest that the tropical Pacific will exert
618 a stronger influence on the Atlantic variability in the future (i.e. a larger reduction
619 in total variance in the NAO region when the tropical Pacific is removed), with three
620 potential mechanisms for this change are presented in [Drouard and Cassou \(2019\)](#). Fur-
621 thermore, models do not agree on future changes in variance for the NAO, reinforcing
622 the idea that this mode remains a key source of uncertainty.

623 Finally, our projections for the tropical Pacific are in agreement with earlier find-
624 ings ([Maher et al, 2023](#)), showing model-dependent changes over time. These include
625 known biases in tropical Pacific variability, consistent with those identified by [Planton
626 et al \(2021\)](#) and [Bellenger et al \(2014\)](#), and contribute to the broader uncertainty in
627 teleconnection patterns under climate change.

628

629 5 Conclusions

630

631 In summary, we find the following:

632

- 633 1. Climate models generally capture the key modes of atmospheric circulation vari-
634 ability in the North Pacific and North Atlantic, with well-known biases remaining
635 in the modes of tropical Pacific SST variability (Figures 3, 4 & S1).
- 636 2. There is limited model agreement on projections of the NPO and NAO. While some
637 of the model disagreement in the NPO can be attributed to differences in tropical
638 Pacific variability, this does not fully account for the spread (Figures 5, 9 & 11).
- 639 3. Most models agree on projected changes in the PNA, which are largely associated
640 with an intensification of the Aleutian low variability. Where this intensification
641 does not occur (e.g. in MIROC6), it can be linked to different behaviour in tropical
642 Pacific variability (Figures 5, 9, 11 & S10).

643

644

4. The EPP is found to contribute to a consistent increase in precipitation variability over California in future projections, suggesting that its influence on this region will strengthen in a warming climate (Figure 12).
5. The effect of all four circulation modes of variability on the south-east US precipitation is masked by the tropical Pacific (Figure 12).
6. Strong links between modes and across basins underscore the difficulty of isolating the effects of individual modes. This highlights the interconnected nature of the climate system (Figures 5, 6, 9, 10).
7. The percentage of variance explained by each mode remains relatively stable in the future, although the total variance may increase or decrease depending on the region and model (Figure 7).
8. Projected precipitation changes are strongly linked to changes in the behaviour and influence of circulation modes, reflecting both direct thermodynamic responses to warming and dynamically mediated impacts (Figures 1, 2).

Acknowledgements. NM was supported by the Australian Research Council Discovery Early Career Researcher Award DE230100315. We would like to acknowledge computing support from the Casper system (<https://ncar.pub/casper>) provided by the National Science Foundation (NSF) National Center for Atmospheric Research (NCAR), sponsored by NSF. We additionally thank Adam Phillips (NSF-NCAR) for providing observational data and guidance. CD is supported by NSF-NCAR. Support for the Twentieth Century Reanalysis Project version 3 dataset is provided by the U.S. Department of Energy, Office of Science Biological and Environmental Research (BER), by the National Oceanic and Atmospheric Administration Climate Program Office, and by the NOAA Earth System Research Laboratory Physical Sciences Laboratory.

Competing Interests. The authors declare no competing interests.

Data availability. SMILE data used in this study is publicly available via the Multi-model large ensemble archive version 2 (MMLEAv2) at <https://www.cesm.ucar.edu/community-projects/mmlea/v2>.

Code availability. All final code will be made available on acceptance on: <https://github.com/nicolamaher>.

Funding. This work was funded by the Australian Research Council Discovery Early Career Researcher Award DE230100315.

Author contribution. This project was co-designed by NM, CD and JPO as a follow up to a previous study by JPO and CD. NM led the project, created the figures and wrote the manuscript. CD and JPO provided input and ideas for the Figures, methods, and helped to synthesise the results. The SEOF code used in the paper was originally written by JPO and modified for use with multiple SMILEs by NM. All authors contributed to the final manuscript.

691 **References**

- 692
693 Barnston AG, Livezey RE (1987) Classification, seasonality and persistence
694 of low-frequency atmospheric circulation patterns. *Monthly Weather Review*
695 115(6):1083 – 1126. [https://doi.org/10.1175/1520-0493\(1987\)115\(1083:CSAPOL\)2.](https://doi.org/10.1175/1520-0493(1987)115(1083:CSAPOL)2.0.CO;2)
696 [0.CO;2](https://doi.org/10.1175/1520-0493(1987)115(1083:CSAPOL)2.0.CO;2), URL [https://journals.ametsoc.org/view/journals/mwre/115/6/1520-0493_](https://journals.ametsoc.org/view/journals/mwre/115/6/1520-0493_1987_115_1083_csapol_2_0_co_2.xml)
697 [1987_115_1083_csapol_2_0_co_2.xml](https://journals.ametsoc.org/view/journals/mwre/115/6/1520-0493_1987_115_1083_csapol_2_0_co_2.xml)
- 698
699 Bellenger H, Guilyardi E, Leloup J, et al (2014) Enso representation in climate models:
700 from cmip3 to cmip5. *Climate Dynamics* 42(7):1999–2018. <https://doi.org/10.1007/s00382-013-1783-z>,
701 URL <https://doi.org/10.1007/s00382-013-1783-z>
- 702
703 Beverley JD, Collins M, Lambert FH, et al (2024) Drivers of changes
704 to the enso–europe teleconnection under future warming. *Geophysical*
705 *Research Letters* 51(10):e2023GL107957. <https://doi.org/https://doi.org/10.1029/2023GL107957>,
706 URL <https://agupubs.onlinelibrary.wiley.com/doi/abs/10.1029/2023GL107957>,
707 [e2023GL107957](https://agupubs.onlinelibrary.wiley.com/doi/abs/10.1029/2023GL107957) 2023GL107957,
708 <https://agupubs.onlinelibrary.wiley.com/doi/pdf/10.1029/2023GL107957>
- 709
710 Boucher O, Servonnat J, Albright AL, et al (2020) Presentation and Eval-
711 uation of the IPSL-CM6A-LR Climate Model. *Journal of Advances in*
712 *Modeling Earth Systems* 12(7):e2019MS002010. <https://doi.org/https://doi.org/10.1029/2019MS002010>,
713 URL <https://agupubs.onlinelibrary.wiley.com/doi/abs/10.1029/2019MS002010>,
714 [e2019MS002010](https://agupubs.onlinelibrary.wiley.com/doi/abs/10.1029/2019MS002010) 10.1029/2019MS002010,
715 <https://agupubs.onlinelibrary.wiley.com/doi/pdf/10.1029/2019MS002010>
- 716
717 Branstator G, Selten F (2009) “modes of variability” and climate change. *Journal of*
718 *Climate* 22(10):2639 – 2658. <https://doi.org/10.1175/2008JCLI2517.1>, URL <https://journals.ametsoc.org/view/journals/clim/22/10/2008jcli2517.1.xml>
- 719
720 Cai W, Santoso A, Collins M, et al (2021) Changing el niño-southern oscil-
721 lation in a warming climate. *Nature Reviews Earth Environment* 2(9):628–
722 644. <https://doi.org/10.1038/s43017-021-00199-z>, URL <https://doi.org/10.1038/s43017-021-00199-z>
- 723
724
725 Cai W, Ng B, Wang G, et al (2022) Increased enso sea surface temperature
726 variability under four ipcc emission scenarios. *Nature Climate Change* 12(3):228–
727 231. <https://doi.org/10.1038/s41558-022-01282-z>, URL <https://doi.org/10.1038/s41558-022-01282-z>
- 728
729
730 Chang P, Fu D, Liu X, et al (2026) Future extreme precipitation amplified by
731 intensified mesoscale moisture convergence. *Nature Geoscience* 19(1):33–41. URL
732 <https://doi.org/10.1038/s41561-025-01859-1>
- 733
734
735
736 Chen S, Yu B, Wu R, et al (2021) The dominant north pacific atmospheric cir-
737 culation patterns and their relations to pacific ssts: historical simulations and
738 future projections in the ipcc ar6 models. *Climate Dynamics* 56(3):701–725. URL

https://doi.org/10.1007/s00382-020-05501-1	737
	738
Chen Z, Gan B, Wu L, et al (2018) Pacific-north american teleconnection and north pacific oscillation: historical simulation and future projection in cmip5 models. <i>Climate Dynamics</i> 50(11):4379–4403. URL https://doi.org/10.1007/s00382-017-3881-9	739
	740
	741
	742
Delworth TL, Cooke WF, Adcroft A, et al (2020) SPEAR: The Next Generation GFDL Modeling System for Seasonal to Multidecadal Prediction and Projection. <i>Journal of Advances in Modeling Earth Systems</i> 12(3):e2019MS001895. https://doi.org/https://doi.org/10.1029/2019MS001895	743
	744
	745
	746
	747
Deser C, Hurrell JW, Phillips AS (2017) The role of the north atlantic oscillation in european climate projections. <i>Climate Dynamics</i> 49(9):3141–3157. URL https://doi.org/10.1007/s00382-016-3502-z	748
	749
	750
	751
Deser C, Simpson IR, Phillips AS, et al (2018) How well do we know enso’s climate impacts over north america, and how do we evaluate models accordingly? <i>Journal of Climate</i> 31(13):4991 – 5014. https://doi.org/10.1175/JCLI-D-17-0783.1 , URL https://journals.ametsoc.org/view/journals/clim/31/13/jcli-d-17-0783.1.xml	752
	753
	754
	755
Deser C, Lehner F, Rodgers KB, et al (2020) Insights from earth system model initial-condition large ensembles and future prospects. <i>Nature Climate Change</i> 10(4):277–286. https://doi.org/10.1038/s41558-020-0731-2	756
	757
	758
	759
Drouard M, Cassou C (2019) A modeling- and process-oriented study to investigate the projected change of enso-forced wintertime teleconnectivity in a warmer world. <i>Journal of Climate</i> 32(23):8047 – 8068. https://doi.org/10.1175/JCLI-D-18-0803.1 , URL https://journals.ametsoc.org/view/journals/clim/32/23/jcli-d-18-0803.1.xml	760
	761
	762
	763
	764
Feldstein SB (2000) The timescale, power spectra, and climate noise properties of teleconnection patterns. <i>Journal of Climate</i> 13(24):4430 – 4440. <a href="https://doi.org/10.1175/1520-0442(2000)013<4430:TTPSAC>2.0.CO;2">https://doi.org/10.1175/1520-0442(2000)013<4430:TTPSAC>2.0.CO;2 , URL https://journals.ametsoc.org/view/journals/clim/13/24/1520-0442_2000_013_4430.ttpsac_2.0.co_2.xml	765
	766
	767
	768
	769
Feldstein SB, Franzke CLE (2017) <i>Atmospheric Teleconnection Patterns</i> , Cambridge University Press, p 54–104	770
	771
	772
Gillett NP, Graf HF, Osborn TJ (2003) Climate Change and the North Atlantic Oscillation, American Geophysical Union (AGU), pp 193–209. https://doi.org/https://doi.org/10.1029/134GM09 , URL https://agupubs.onlinelibrary.wiley.com/doi/abs/10.1029/134GM09 , https://agupubs.onlinelibrary.wiley.com/doi/pdf/10.1029/134GM09	773
	774
	775
	776
	777
	778
Haszpra T, Herein M, Bódai T (2020) Investigating enso and its teleconnections under climate change in an ensemble view – a new perspective. <i>Earth System Dynamics</i> 11(1):267–280. https://doi.org/10.5194/esd-11-267-2020 , URL https://esd.copernicus.org/articles/11/267/2020/	779
	780
	781
	782

- 783 Herein M, Márffy J, Drótos G, et al (2016) Probabilistic concepts in intermediate-
784 complexity climate models: A snapshot attractor picture. *Journal of Climate*
785 29(1):259 – 272. <https://doi.org/10.1175/JCLI-D-15-0353.1>, URL [https://journals.
786 ametsoc.org/view/journals/clim/29/1/jcli-d-15-0353.1.xml](https://journals.ametsoc.org/view/journals/clim/29/1/jcli-d-15-0353.1.xml)
787
- 788 Huang B, Thorne PW, Banzon VF, et al (2017) Extended reconstructed sea sur-
789 face temperature, version 5 (ersstv5): Upgrades, validations, and intercomparisons.
790 *Journal of Climate* 30(20):8179 – 8205. <https://doi.org/10.1175/JCLI-D-16-0836.1>,
791 URL <https://journals.ametsoc.org/view/journals/clim/30/20/jcli-d-16-0836.1.xml>
792
- 793 Huang Y, Ren HL, Chadwick R, et al (2018) Diagnosing changes of winter nao
794 in response to different climate forcings in a set of atmosphere-only timeslice
795 experiments. *Atmosphere* 9(1). <https://doi.org/10.3390/atmos9010010>, URL [https:
796 //www.mdpi.com/2073-4433/9/1/10](https://www.mdpi.com/2073-4433/9/1/10)
797
- 798 Hurrell JW, Kushnir Y, Ottersen G, et al (2003) An Overview of the North
799 Atlantic Oscillation, American Geophysical Union (AGU), pp 1–35. [https://doi.
800 org/https://doi.org/10.1029/134GM01](https://doi.org/https://doi.org/10.1029/134GM01), URL [https://agupubs.onlinelibrary.wiley.
801 com/doi/abs/10.1029/134GM01](https://agupubs.onlinelibrary.wiley.com/doi/abs/10.1029/134GM01), [https://agupubs.onlinelibrary.wiley.com/doi/pdf/
802 10.1029/134GM01](https://agupubs.onlinelibrary.wiley.com/doi/pdf/10.1029/134GM01)
803
- 804 Kay JE, Deser C, Phillips A, et al (2015) The Community Earth System Model
805 (CESM) Large Ensemble Project: A Community Resource for Studying Climate
806 Change in the Presence of Internal Climate Variability. *Bulletin of American Mete-
807 orological Society* 96(8):1333–1349. <https://doi.org/10.1175/BAMS-D-13-00255.1>
808
- 809 Lee JJ.-Y., Marotzke, Bala G, et al (2021) Climate Change 2021: The Physical Science
810 Basis. Contribution of Working Group I to the Sixth Assessment Report of the
811 Intergovernmental Panel on Climate Change, Cambridge University Press, chap
812 Future Global Climate: Scenario-Based Projections and NearTerm Information, pp
813 553–672. <https://doi.org/10.1017/9781009157896.006>
814
- 815 Linkin ME, Nigam S (2008) The north pacific oscillation–west pacific teleconnection
816 pattern: Mature-phase structure and winter impacts. *Journal of Climate* 21(9):1979
817 – 1997. <https://doi.org/10.1175/2007JCLI2048.1>, URL [https://journals.ametsoc.
818 org/view/journals/clim/21/9/2007jcli2048.1.xml](https://journals.ametsoc.org/view/journals/clim/21/9/2007jcli2048.1.xml)
819
- 819 Maher N, Matei D, Milinski S, et al (2018) ENSO Change in Climate Projections:
820 Forced Response or Internal Variability? *Geophysical Research Letters* 45:11,390–
821 11,398. <https://doi.org/10.1029/2018GL079764>
822
- 823 Maher N, Milinski S, Suarez-Gutierrez L, et al (2019) The Max Planck Institute
824 Grand Ensemble: Enabling the Exploration of Climate System Variability. *Journal
825 of Advances in Modeling Earth Systems* 11(7):2050–2069. [https://doi.org/10.1029/
826 2019MS001639](https://doi.org/10.1029/2019MS001639)
827
828

Maher N, Milinski S, Ludwig R (2021a) Large ensemble climate model simulations: introduction, overview, and future prospects for utilising multiple types of large ensemble. <i>Earth System Dynamics</i> 12(2):401–418. https://doi.org/10.5194/esd-12-401-2021 , URL https://esd.copernicus.org/articles/12/401/2021/	829 830 831 832 833
Maher N, Power SB, Marotzke J (2021b) More accurate quantification of model-to-model agreement in externally forced climatic responses over the coming century. <i>Nature Communications</i> 12(1):788. URL https://doi.org/10.1038/s41467-020-20635-w	834 835 836 837 838
Maher N, Kay JE, Capotondi A (2022) Modulation of enso teleconnections over north america by the pacific decadal oscillation. <i>Environmental Research Letters</i> 17(11):114005. https://doi.org/10.1088/1748-9326/ac9327 , URL https://dx.doi.org/10.1088/1748-9326/ac9327	839 840 841 842 843
Maher N, Wills RCJ, DiNezio P, et al (2023) The future of the el niño–southern oscillation: using large ensembles to illuminate time-varying responses and inter-model differences. <i>Earth System Dynamics</i> 14(2):413–431. https://doi.org/10.5194/esd-14-413-2023 , URL https://esd.copernicus.org/articles/14/413/2023/	844 845 846 847 848
Maher N, Phillips AS, Deser C, et al (2025) The updated multi-model large ensemble archive and the climate variability diagnostics package: New tools for the study of climate variability and change. <i>Geoscientific Model Development</i> 18:6341–6365. https://doi.org/https://doi.org/10.5194/gmd-18-6341-2025	849 850 851 852 853
McGregor S, Cassou C, Kosaka Y, et al (2022) Projected enso teleconnection changes in cmip6. <i>Geophysical Research Letters</i> 49(11):e2021GL097511. https://doi.org/https://doi.org/10.1029/2021GL097511 , URL https://agupubs.onlinelibrary.wiley.com/doi/abs/10.1029/2021GL097511 , e2021GL097511 2021GL097511, https://agupubs.onlinelibrary.wiley.com/doi/pdf/10.1029/2021GL097511	854 855 856 857 858
McKenna CM, Maycock AC (2021) Sources of uncertainty in multimodel large ensemble projections of the winter north atlantic oscillation. <i>Geophysical Research Letters</i> 48(14):e2021GL093258. https://doi.org/https://doi.org/10.1029/2021GL093258 , URL https://agupubs.onlinelibrary.wiley.com/doi/abs/10.1029/2021GL093258 , e2021GL093258 2021GL093258, https://agupubs.onlinelibrary.wiley.com/doi/pdf/10.1029/2021GL093258	859 860 861 862 863 864 865
Michel C, Li C, Simpson IR, et al (2020) The change in the enso teleconnection under a low global warming scenario and the uncertainty due to internal variability. <i>Journal of Climate</i> 33(11):4871 – 4889. https://doi.org/10.1175/JCLI-D-19-0730.1 , URL https://journals.ametsoc.org/view/journals/clim/33/11/jcli-d-19-0730.1.xml	866 867 868 869 870
Newman M, Alexander MA, Ault TR, et al (2016) The pacific decadal oscillation, revisited. <i>Journal of Climate</i> 29(12):4399 – 4427. https://doi.org/10.1175/JCLI-D-15-0508.1 , URL https://journals.ametsoc.org/view/journals/clim/29/12/jcli-d-15-0508.1.xml	871 872 873 874

- 875 O'Brien JP, Deser C (2023) Quantifying and understanding forced changes to
876 unforced modes of atmospheric circulation variability over the north pacific in
877 a coupled model large ensemble. *Journal of Climate* 36(1):19 – 37. <https://doi.org/10.1175/JCLI-D-22-0101.1>, URL <https://journals.ametsoc.org/view/journals/clim/36/1/JCLI-D-22-0101.1.xml>
880
- 881 Planton YY, Guilyardi E, Wittenberg AT, et al (2021) Evaluating Climate Models with
882 the CLIVAR 2020 ENSO Metrics Package. *Bulletin of the American Meteorological Society* 102(2):E193 – E217. <https://doi.org/10.1175/BAMS-D-19-0337.1>, URL
883 <https://journals.ametsoc.org/view/journals/bams/102/2/BAMS-D-19-0337.1.xml>
884
- 885 Planton YY, Lee J, Wittenberg AT, et al (2024) Estimating uncertainty in simulated enso statistics. *Journal of Advances in Modeling Earth Systems* 16(9):e2023MS004147. <https://doi.org/https://doi.org/10.1029/2023MS004147>, URL <https://agupubs.onlinelibrary.wiley.com/doi/abs/10.1029/2023MS004147>, e2023MS004147 2023MS004147,
886 <https://agupubs.onlinelibrary.wiley.com/doi/pdf/10.1029/2023MS004147>
887
- 888 Power S, Delage F, Chung C, et al (2013) Robust twenty-first-century projections of
889 elniño and related precipitation variability. *Nature* 502(7472):541–545. <https://doi.org/10.1038/nature12580>, URL <https://doi.org/10.1038/nature12580>
890
- 891 Risbey JS, Pook MJ, McIntosh PC, et al (2009) On the remote drivers of rainfall
892 variability in australia. *Monthly Weather Review* 137(10):3233 – 3253. <https://doi.org/10.1175/2009MWR2861.1>, URL <https://journals.ametsoc.org/view/journals/mwre/137/10/2009mwr2861.1.xml>
893
- 894 Rodgers KB, Lee SS, Rosenbloom N, et al (2021) Ubiquity of human-induced changes
895 in climate variability. *Earth System Dynamics* 12(4):1393–1411. <https://doi.org/10.5194/esd-12-1393-2021>, URL <https://esd.copernicus.org/articles/12/1393/2021/>
896
- 897 Shepherd TG (2014) Atmospheric circulation as a source of uncertainty in climate
898 change projections. *Nature Geoscience* 7(10):703–708. URL <https://doi.org/10.1038/ngeo2253>
899
- 900 Simpson IR, Shaw TA, Ceppi P, et al (2025) Confronting earth system
901 model trends with observations. *Science Advances* 11(11):eadt8035. <https://doi.org/10.1126/sciadv.adt8035>, URL <https://www.science.org/doi/abs/10.1126/sciadv.adt8035>, <https://www.science.org/doi/pdf/10.1126/sciadv.adt8035>
902
- 903 Smith DM, Dunstone NJ, Eade R, et al (2025) Mitigation needed to avoid unprece-
904 dented multi-decadal north atlantic oscillation magnitude. *Nature Climate Change* 15(4):403–410. URL <https://doi.org/10.1038/s41558-025-02277-2>
905
- 906 Suarez-Gutierrez L, Milinski S, Maher N (2021) Exploiting large ensembles for a better
907 yet simpler climate model evaluation. *Climate Dynamics* 57(9):2557–2580. URL
908 <https://doi.org/10.1007/s00382-021-05821-w>
909
- 910
- 911
- 912
- 913
- 914
- 915
- 916
- 917
- 918
- 919
- 920

Swart NC, Cole JNS, Kharin VV, et al (2019) The Canadian Earth System Model version 5 (CanESM5.0.3). *Geoscientific Model Development* 12(11):4823–4873. <https://doi.org/10.5194/gmd-12-4823-2019>, URL <https://gmd.copernicus.org/articles/12/4823/2019/>

Takahashi K, Montecinos A, Goubanova K, et al (2011) Enso regimes: Reinterpreting the canonical and modoki el niño. *Geophysical Research Letters* 38(10). <https://doi.org/https://doi.org/10.1029/2011GL047364>, URL <https://agupubs.onlinelibrary.wiley.com/doi/abs/10.1029/2011GL047364>, <https://agupubs.onlinelibrary.wiley.com/doi/pdf/10.1029/2011GL047364>

Tatebe H, Ogura T, Nitta T, et al (2019) Description and basic evaluation of simulated mean state, internal variability, and climate sensitivity in MIROC6. *Geoscientific Model Development* 12(7):2727–2765. <https://doi.org/10.5194/gmd-12-2727-2019>, URL <https://gmd.copernicus.org/articles/12/2727/2019/>

Visbeck MH, Hurrell JW, Polvani L, et al (2001) The north atlantic oscillation: Past, present, and future. *Proceedings of the National Academy of Sciences* 98(23):12876–12877. <https://doi.org/10.1073/pnas.231391598>, URL <https://www.pnas.org/doi/abs/10.1073/pnas.231391598>, <https://www.pnas.org/doi/pdf/10.1073/pnas.231391598>

Wallace JM, Gutzler DS (1981) Teleconnections in the geopotential height field during the northern hemisphere winter. *Monthly Weather Review* 109(4):784 – 812. [https://doi.org/10.1175/1520-0493\(1981\)109<0784:TITGHF>2.0.CO;2](https://doi.org/10.1175/1520-0493(1981)109<0784:TITGHF>2.0.CO;2), URL https://journals.ametsoc.org/view/journals/mwre/109/4/1520-0493-1981_109_0784_titghf_2_0_co_2.xml

Wengel C, Lee SS, Stuecker MF, et al (2021) Future high-resolution el niño/southern oscillation dynamics. *Nature Climate Change* 11(9):758–765. <https://doi.org/10.1038/s41558-021-01132-4>, URL <https://doi.org/10.1038/s41558-021-01132-4>

van der Wiel K, Bintanja R (2021) Contribution of climatic changes in mean and variability to monthly temperature and precipitation extremes. *Communications Earth & Environment* 2(1):1. URL <https://doi.org/10.1038/s43247-020-00077-4>

Yuan J, Tan B, Feldstein SB, et al (2015) Wintertime north pacific teleconnection patterns: Seasonal and interannual variability. *Journal of Climate* 28(20):8247 – 8263. <https://doi.org/10.1175/JCLI-D-14-00749.1>, URL <https://journals.ametsoc.org/view/journals/clim/28/20/jcli-d-14-00749.1.xml>

Zhou ZQ, Xie SP, Zheng XT, et al (2014) Global warming-induced changes in el niño teleconnections over the north pacific and north america. *Journal of Climate* 27(24):9050 – 9064. <https://doi.org/10.1175/JCLI-D-14-00254.1>, URL <https://journals.ametsoc.org/view/journals/clim/27/24/jcli-d-14-00254.1.xml>

967 Ziehn T, Chamberlain MA, Law RM, et al (2020) The Australian Earth System Model:
 968 ACCESS-ESM1.5. JSHESS 70(1):193-214. URL <https://doi.org/10.1071/ES19035>

969

970

971

972

973

974

975

976

977

978

979

980

981

982

983

984

985

986

987

988

989

990

991

992

993

994

995

996

997

998

999

1000

1001

1002

1003

1004

1005

1006

1007

1008

1009

1010

1011

1012

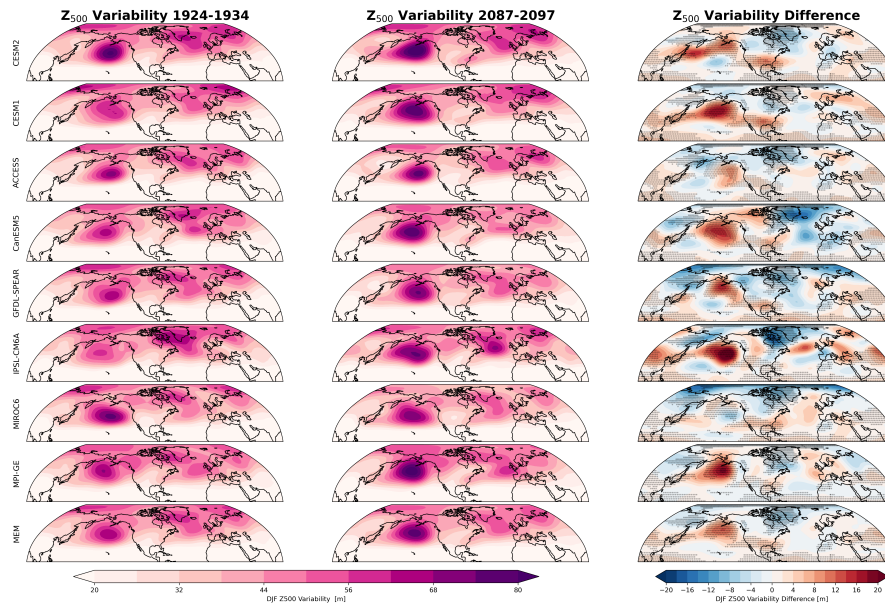


Fig. 1 Projected change in 500hPa geopotential height (Z500) variability across SMILEs. Z500 variability is calculated as a standard deviation across the ensemble for (left) the early period (1924-1934), (middle) the late period (2087-2097), and (right) their difference (late minus early) for each SMILE and the multi-ensemble mean (MEM). Stippling in the right column shows where at least 7 SMILEs agree on the sign of the projected change. The variability in each decade is based on individual DJF seasons, not decadal averages, and the MEM results are based on computing the mean standard deviation by taking the square-root of the mean variance across models.

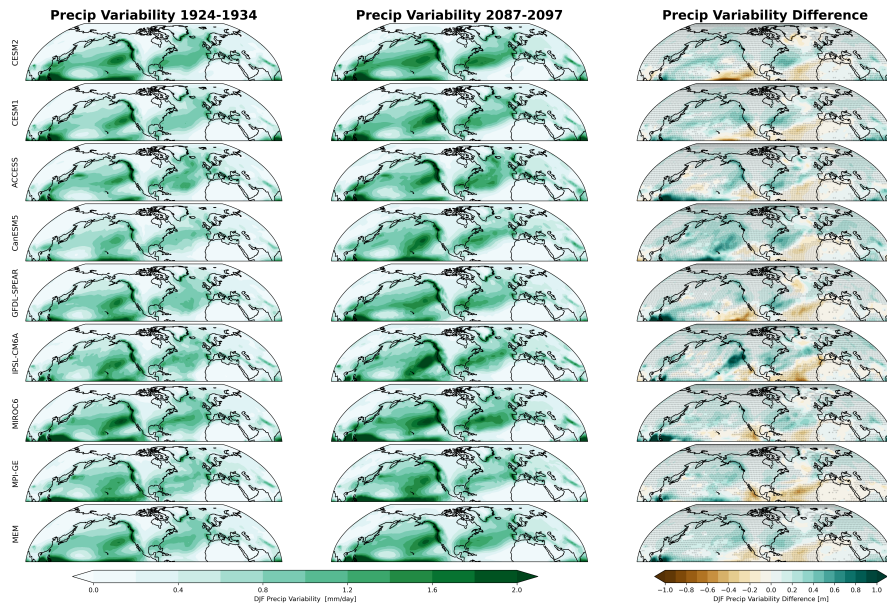


Fig. 2 Projected change in precipitation variability across SMILEs. As in Figure 1 except for precipitation variability.

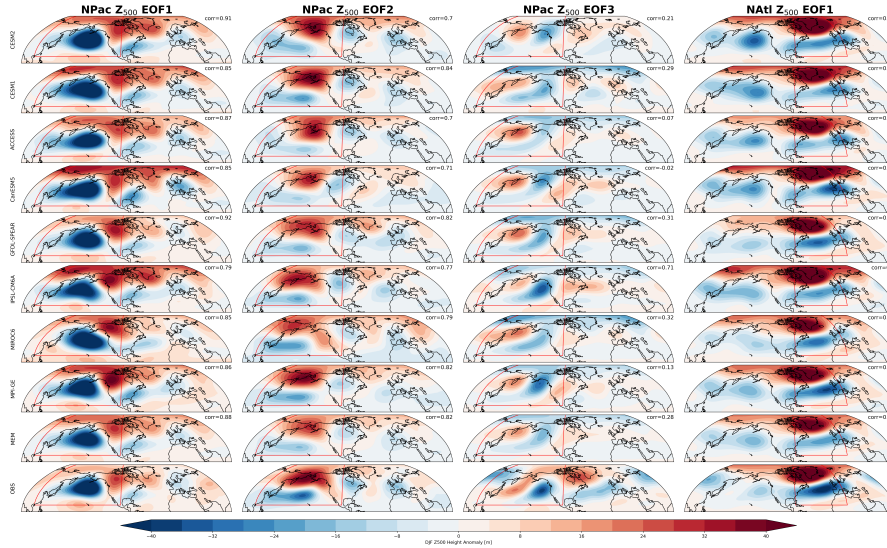


Fig. 3 Traditional (time-based) EOFs of Z500 variability over the North Pacific and Atlantic for the historical period (1950-2015) for the 8 SMILEs, the multi-ensemble mean (MEM, computed as the average of the eight SMILE regression maps) and observations from NOAA/CIRES/DOE 20th Century Reanalysis (V3). Observations are detrended by removing a quadratically fitted polynomial from each grid point, while the SMILEs are detrended by removing the ensemble mean. The pattern correlation of each map with the observed map for the domains where the EOFs are computed (illustrated using the red box) is shown in the top right corner of each subplot. The EOFs for tropical Pacific SST variability are shown in Figure S1. SEOFs for the same period are shown in Figure S2 for comparison.

1059
 1060
 1061
 1062
 1063
 1064
 1065
 1066
 1067
 1068
 1069
 1070
 1071
 1072
 1073
 1074
 1075
 1076
 1077
 1078
 1079
 1080
 1081
 1082
 1083
 1084
 1085
 1086
 1087
 1088
 1089
 1090
 1091
 1092
 1093
 1094
 1095
 1096
 1097
 1098
 1099
 1100
 1101
 1102
 1103
 1104

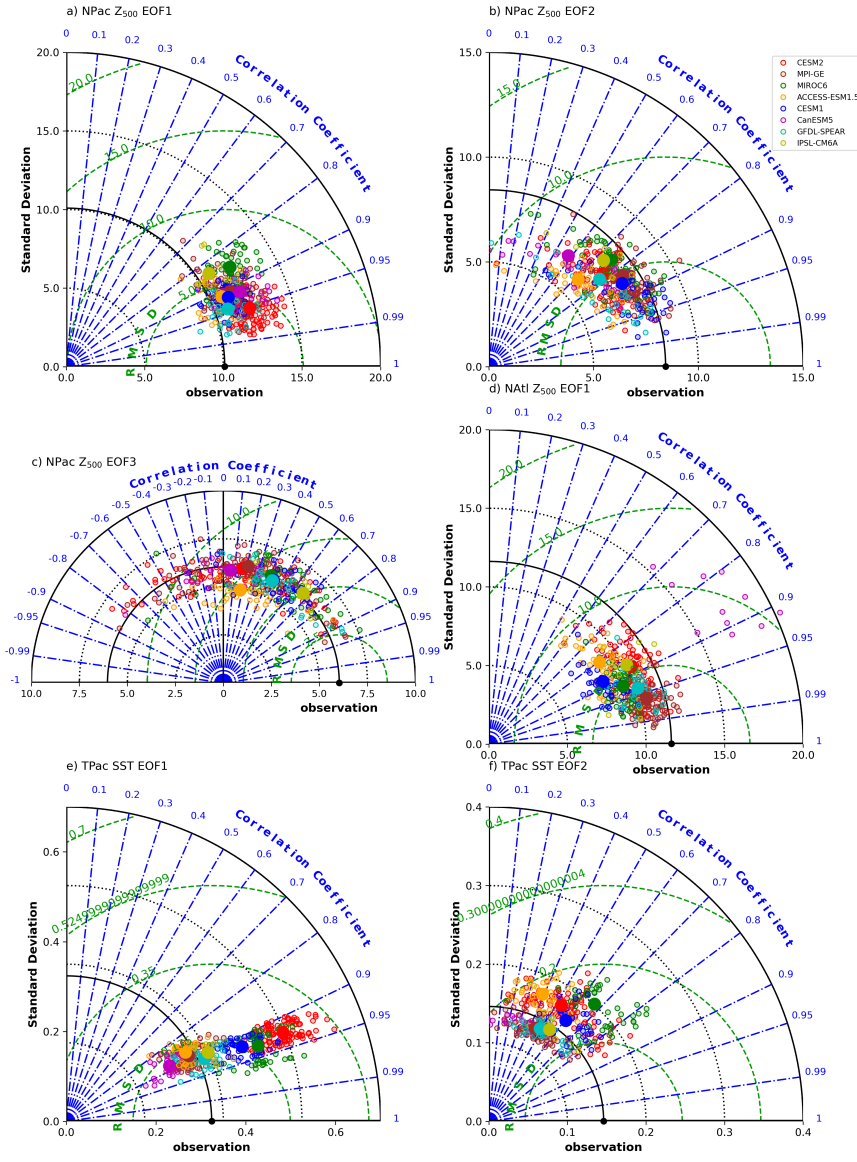


Fig. 4 Taylor diagram for each SMILE EOF compared to observations. Shown for North Pacific Z500 EOFs 1-3, North Atlantic Z500 EOF1 and Tropical Pacific SST EOFs 1-2. The Taylor diagram shows each SMILE in a different colour with the small dots individual ensemble members and the large dot the ensemble mean. Observations are shown in black. Z500 observations are from NOAA/CIRES/DOE 20th Century Reanalysis (V3) (1950-2015) and SST observations are from ERSSTv5 (1950-2015) (Huang et al, 2017). For this plot the EOFs are computed against time for the same period as the observations for each ensemble member. The plot shows the pattern correlation with observations in blue lines, the root mean squared difference (RMSD) in green circles and the standard deviation in black. Higher correlations, lower RMSD and a standard deviation close to the black observational dot indicate that the model is closer to observations. For this analysis the forced response is removed from the SMILE by removing the ensemble mean at each timestep. The observations are detrended using a quadratic fit. We note that detrending the SMILEs by removing a quadratic fit gives a qualitatively similar answer (not shown). The EOF patterns for both observations and SMILEs used in this Figure are shown in Figure S3.

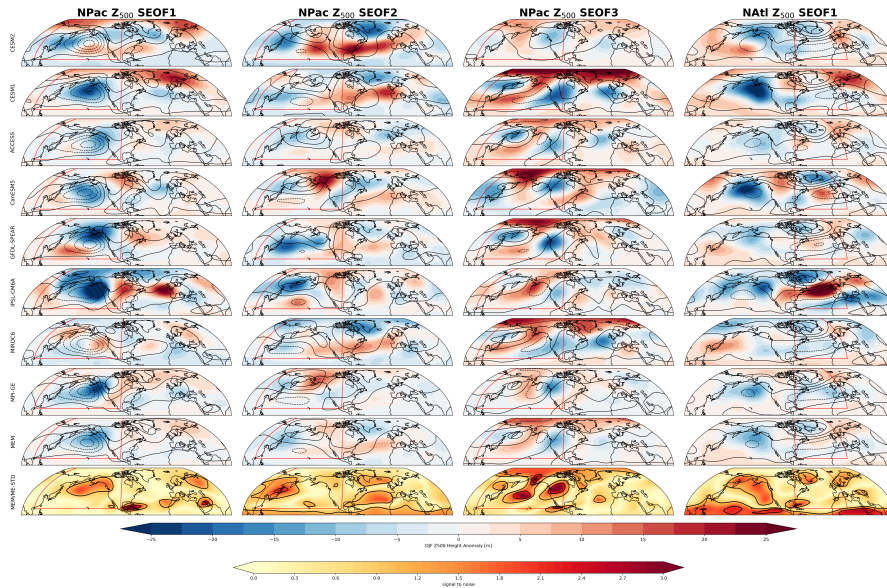


Fig. 5 Projected change in the North Pacific and North Atlantic Z500 SEOFs regressed back onto Z500. Each SEOF is regressed onto Z500 in DJF. Shown is the change in this regression in 2087-2097 compared to 1924-1934. Shown for each SMILE, the multi-ensemble mean (MEM) and the signal-to-noise ratio defined as the MEM divided by the standard deviation across the 8 SMILE means (ME-STD). Contours show the baseline period 1924-1934 for reference. Contours on the signal-to-noise ratio show the values 1 and 2. Full projection for the later period is shown in Figure S4.

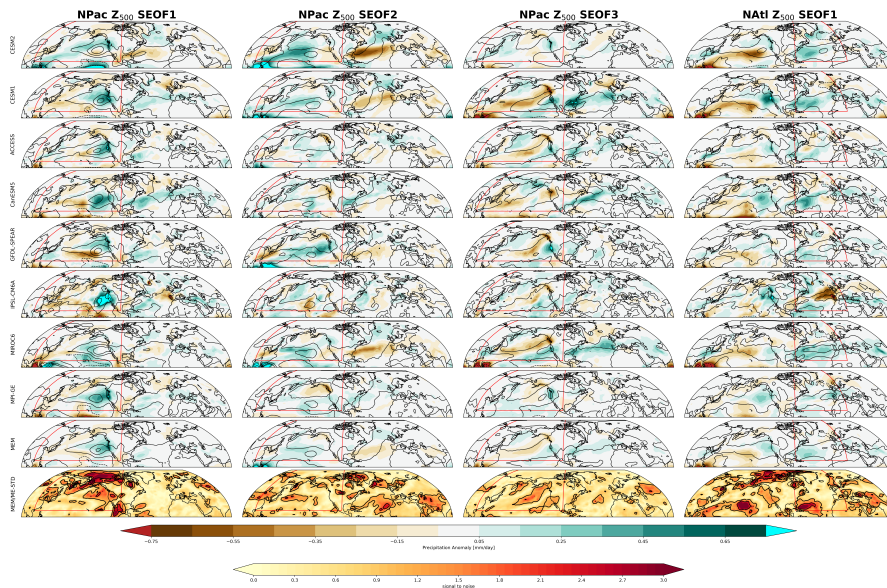
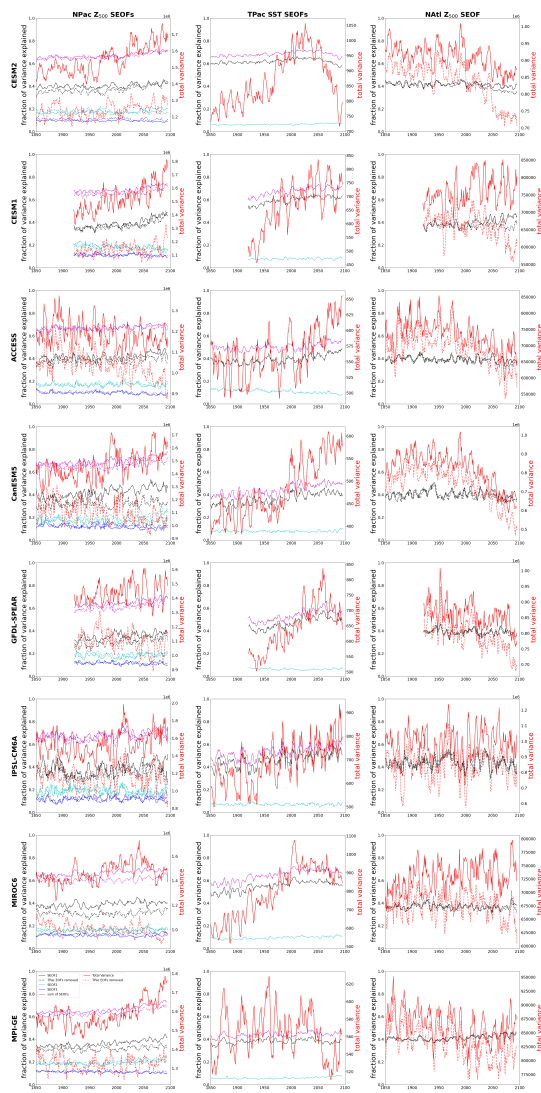


Fig. 6 Projected change in the North Pacific and North Atlantic Z500 SEOFs regressed onto precipitation. As in Figure 5 except for precipitation. Full projection for the later period is shown in Figure S5.

1105
1106
1107
1108
1109
1110
1111
1112
1113
1114
1115
1116
1117
1118
1119
1120
1121
1122
1123
1124
1125
1126
1127
1128
1129
1130
1131
1132
1133
1134
1135
1136
1137
1138
1139
1140
1141
1142
1143
1144
1145
1146
1147
1148
1149
1150

1151
 1152
 1153
 1154
 1155
 1156
 1157
 1158
 1159
 1160
 1161
 1162
 1163
 1164
 1165
 1166
 1167
 1168
 1169
 1170
 1171
 1172
 1173
 1174
 1175
 1176
 1177
 1178
 1179
 1180
 1181
 1182
 1183
 1184
 1185
 1186
 1187
 1188
 1189
 1190
 1191
 1192
 1193
 1194



1195 **Fig. 7 Variance explained by each SEOF and total variance in each region.** Variance
 1196 explained for each SEOF is shown for each of the 8 SMILES. The total variance is shown in red. For
 the North Pacific and North Atlantic SEOFs the dotted lines indicate the total variance and variance
 explained when the influence of the two tropical Pacific SEOFs are removed. Variance units are the
 square of the original units of the data.

1197
 1198
 1199
 1200
 1201
 1202
 1203
 1204
 1205
 1206
 1207
 1208
 1209
 1210
 1211
 1212
 1213
 1214
 1215
 1216
 1217
 1218
 1219
 1220
 1221
 1222
 1223
 1224
 1225
 1226
 1227
 1228
 1229
 1230
 1231
 1232
 1233
 1234
 1235
 1236
 1237
 1238
 1239
 1240
 1241
 1242

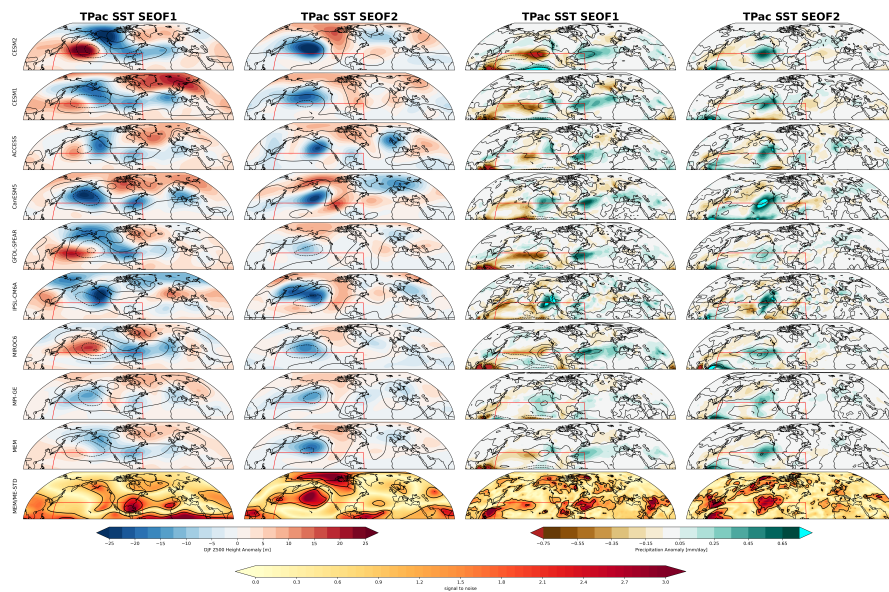
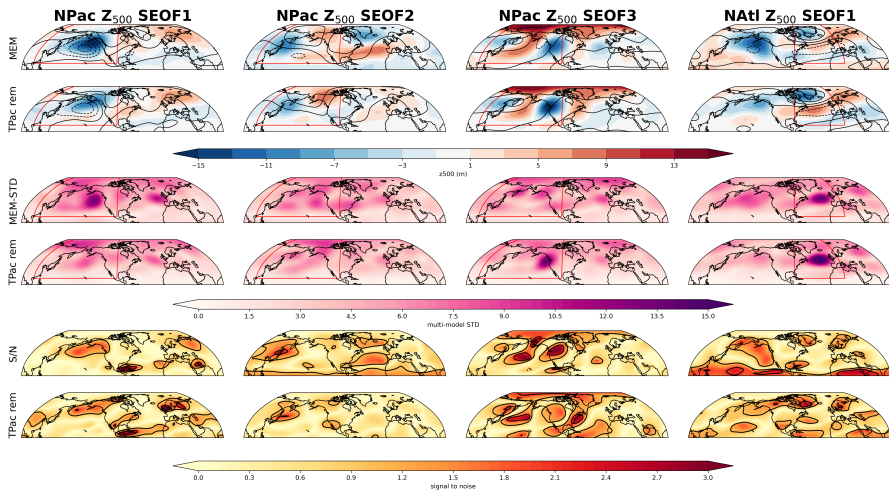


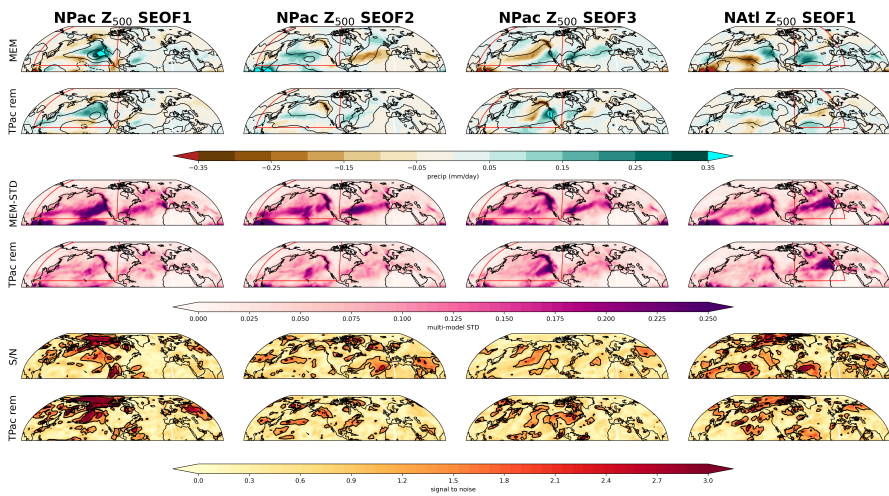
Fig. 8 Projected change in the Tropical Pacific SST EOFs regressed onto Z500 and precipitation. Each EOF is regressed onto Z500 (left) and precipitation (right) in DJF. Shown is the change in this regression in 2087-2097 compared to 1924-1934. Shown for each SMILE, the multi-ensemble mean (MEM) the signal-to-noise ratio defined as the MEM divided by the standard deviation across the 8 SMILE means (ME-STD). Contours show the baseline period 1924-1934 for reference. Contours on the signal-to-noise ratio show the values 1 and 2. Full projections are shown in Figure S6 and S7.

1243
 1244
 1245
 1246
 1247
 1248
 1249
 1250
 1251
 1252
 1253
 1254
 1255
 1256
 1257
 1258
 1259



1260 **Fig. 9 Summary of influence of removing the tropical Pacific SEOFs on Z500.** Each
 1261 SEOF is regressed onto Z500 in DJF. Shown is the change in this regression in 2087-2097 compared
 1262 to 1924-1934. The top two rows show the multi-ensemble mean (MEM) of this change (first row) and
 1263 the change once the influence of the tropical Pacific is removed (second row). Contours show the
 1264 baseline period 1924-1934 for reference. The multi-ensemble STD (ME-STD) of the change is shown
 1265 in the second two rows (first row) and ME-STD once the influence of the tropical Pacific is removed
 1266 (second row). The bottom two rows show the signal-to-noise ratio of the change defined as the MEM
 1267 divided by the standard deviation across the 8 SMILE means (ME-STD) (first row) and once the
 1268 influence of the tropical Pacific is removed (second row). Contours on the signal-to-noise ratio show
 1269 the values 1 and 2. Individual models are shown in Figure S10.

1268
 1269
 1270
 1271
 1272
 1273
 1274
 1275
 1276
 1277
 1278
 1279
 1280
 1281
 1282
 1283
 1284
 1285



1286 **Fig. 10 Summary of influence of removing the tropical Pacific SEOFs on precipitation.**
 1287 Same as Figure 9 except for precipitation. Individual models are shown in Figure S11.

1288

1289
 1290
 1291
 1292
 1293
 1294
 1295
 1296
 1297
 1298
 1299
 1300
 1301
 1302
 1303
 1304
 1305
 1306
 1307
 1308
 1309
 1310
 1311
 1312
 1313
 1314
 1315
 1316
 1317
 1318
 1319
 1320
 1321
 1322
 1323
 1324
 1325
 1326
 1327
 1328
 1329
 1330
 1331
 1332
 1333
 1334

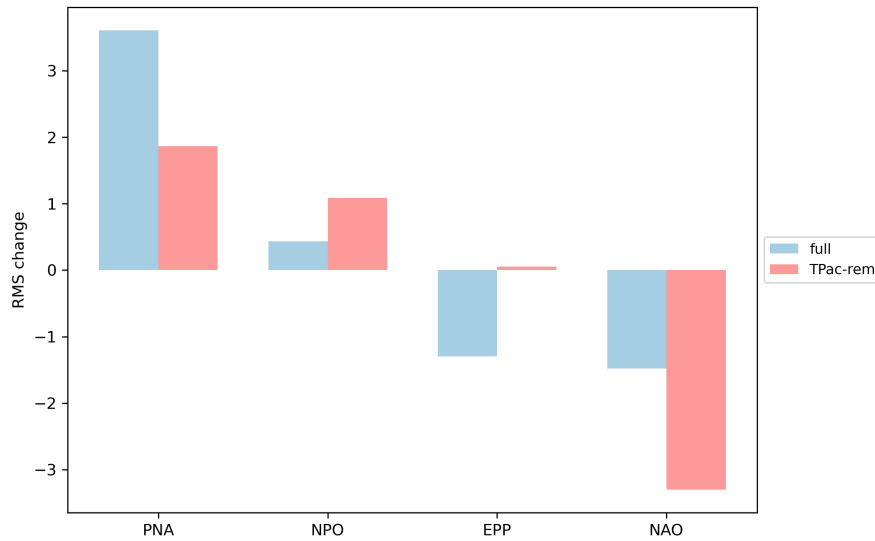


Fig. 11 Change in RMS of the ensemble mean projected change in North Pacific and North Atlantic Z500 SEOFs regressed back onto Z500 for each region itself. Shown for the full projection (blue) and with the tropical Pacific influence regressed out (pink). The change is computed as the RMS in 2087 - 2097 minus the RMS in 1924-1934 over the individual regions that the SEOFs are computed in.

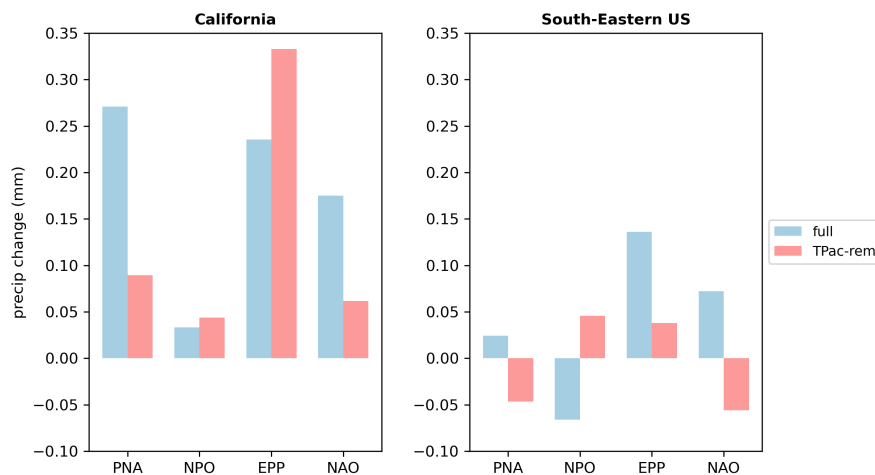


Fig. 12 Californian and South-Eastern US precipitation variability related to each mode and after removing the influence of the leading two modes of tropical Pacific SST variability. Mean precipitation at each timestep over California (left; 234-245E, 31-44N) and the South-Eastern US (right; 270-286E, 24-36N) calculated as a regression of precipitation onto each Z500 mode in each SMILE before (blue) and after (pink) removing the influence of the two leading modes of tropical Pacific SST variability.